Monthly Notices
of the
ROYAL ASTRONOMICAL SOCIETY

MNRAS **492,** 1691–1705 (2020)
Advance Access publication 2020 January 8

doi:10.1093/mnras/stz3520

# Ozone chemistry on tidally locked M dwarf planets

Jack S. Yates,[1,2] Paul I. Palmer,[1,2]★ James Manners,[3] Ian Boutle,[3] Krisztian Kohary,[4] Nathan Mayne[4] and Luke Abraham[5,6]

[1]*School of GeoSciences, University of Edinburgh, King's Buildings, Edinburgh EH9 3FF, UK*
[2]*Centre for Exoplanet Science, University of Edinburgh, Edinburgh EH9 3FD, UK*
[3]*Met Office, Exeter EX1 3PB, UK*
[4]*Astrophysics Group, University of Exeter, Exeter EX4 2QL, UK*
[5]*National Centre for Atmospheric Science, University of Cambridge, Cambridge CB2 1EW, UK*
[6]*Department of Chemistry, University of Cambridge, Cambridge CB2 1EW, UK*

Accepted 2019 December 10. Received 2019 December 9; in original form 2019 June 3

## ABSTRACT

We use the Met Office Unified Model to explore the potential of a tidally locked M dwarf planet, nominally Proxima Centauri b irradiated by a quiescent version of its host star, to sustain an atmospheric ozone layer. We assume a slab ocean surface layer, and an Earth-like atmosphere of nitrogen and oxygen with trace amounts of ozone and water vapour. We describe ozone chemistry using the Chapman mechanism and the hydrogen oxide ($HO_x$, describing the sum of OH and $HO_2$) catalytic cycle. We find that Proxima Centauri radiates with sufficient UV energy to initialize the Chapman mechanism. The result is a thin but stable ozone layer that peaks at 0.75 parts per million at 25 km. The quasi-stationary distribution of atmospheric ozone is determined by photolysis driven by incoming stellar radiation and by atmospheric transport. Ozone mole fractions are smallest in the lowest 15 km of the atmosphere at the substellar point and largest in the nightside gyres. Above 15 km the ozone distribution is dominated by an equatorial jet stream that circumnavigates the planet. The nightside ozone distribution is dominated by two cyclonic Rossby gyres that result in localized ozone hotspots. On the dayside the atmospheric lifetime is determined by the $HO_x$ catalytic cycle and deposition to the surface, with nightside lifetimes due to chemistry much longer than time-scales associated with atmospheric transport. Surface UV values peak at the substellar point with values of 0.01 W $m^{-2}$, shielded by the overlying atmospheric ozone layer but more importantly by water vapour clouds.

**Key words:** astrobiology – planets and satellites: atmospheres.

## 1 INTRODUCTION

We are only just beginning to classify the rapidly growing number of extrasolar planets (exoplanets) that orbit stars outside our solar system. In the absence of other reference points, this classification exercise is guided by the mass and radii of Solar system planets, even though they may not share similar evolutionary pathways (Seager et al. 2007; Spiegel, Fortney & Sotin 2014; Weiss & Marcy 2014). Exoplanets range from scientific curiosities (e.g. COROT-Exo-7b, Léger et al. 2009) to candidates for supporting life (Quintana et al. 2014; Anglada-Escudé et al. 2016; Gillon et al. 2017). Using ever more sophisticated technology, we are now detecting Earth-like exoplanets that receive similar amounts of stellar irradiation as Earth receives from the Sun, placing them into the circumstellar habitable zone (CHZ). From an anthropocentric perspective, the CHZ is a region around the host star that would support liquid water on the planetary surface, a requirement for life (Kasting 1988; Kasting, Whitmire & Reynolds 1993); meeting this criterion means a planet is habitable and not that it is necessarily inhabited. A zeroth-order estimate of the CHZ can be determined from the stellar irradiance and the star–planet distance. However, planetary atmospheres play a significant role in the planetary energy balance depending on atmospheric composition, e.g. infrared absorbers such as greenhouse gases (Meadows & Barnes 2018) and reflecting and absorbing aerosol particles and clouds. Consideration of a planetary atmosphere is therefore integral for understanding whether an exoplanet is habitable. Here, we use the computational framework from a leading 3D Earth system model to describe the interplay between atmospheric dynamics and a simplified description of atmospheric ozone chemistry on a tidally locked M dwarf planet, nominally Proxima Centauri b (Anglada-Escudé et al. 2016). The planet is

★ E-mail: paul.palmer@ed.ac.uk

irradiated by an M dwarf spectrum that is representative of an older, quiescent version of its host star. We use 3D model calculations to study variations in atmospheric ozone and to understand how ozone affects the habitability of the planet, e.g. surface UV environment and broader impacts on climate.

The first detections of planets around main-sequence stars came in 1995 (Mayor & Queloz 1995). In the 2000s, automated surveys revolutionized the field yielding vast quantities of planet detections (e.g. Borucki 2016). To date, thousands of exoplanets have been discovered (e.g. Morton et al. 2016; Thompson et al. 2018) across a broad range of bulk planetary properties. Telescope and detector technologies have already allowed characterization of giant exoplanet atmospheres through transmission (e.g. Sing et al. 2011) and emission (e.g. Todorov et al. 2014) spectroscopy and direct imaging (Lagrange et al. 2010). The first detection of an exoplanet atmosphere was achieved using transmission spectroscopy and showed absorption by the sodium doublet in the atmosphere of the hot Jupiter HD 209458b (Charbonneau et al. 2002). Recent surveys have detected Earth-sized planets on close orbits around cold M dwarf stars, notably Proxima Centauri b (Anglada-Escudé et al. 2016) and the TRAPPIST 1 planets (Gillon et al. 2017). For these planets, orbital distance and low stellar flux compensate for each other, resulting in Earth-like levels of top-of-the-atmosphere radiation, placing them in the CHZ (Kasting et al. 1993).

It is no coincidence that these planets have thus far been detected only around M dwarf stars. These stars represent 70 per cent of all stars (Bochanski et al. 2010), and the detectability of their orbiting planets is greater due to the increased planet-to-star radius ratio. The detectability of a planet also increases as the orbital semimajor axis decreases because of the diminished effect of inclination and the subsequent increased frequency of transits and the larger radial-velocity signature. Demographic studies suggest that M dwarfs are more likely than larger stars to host small planets (Shields, Ballard & Johnson 2016). Collectively, these observational factors suggest that M dwarfs are our best hope for finding exoplanets in the CHZ. However, there are many unknowns in the habitability assessment of a candidate M dwarf, e.g. the manifold impacts of climate on stellar and planetary environments (Shields et al. 2016). Until telescopes are capable of detailed observations of M dwarf planets, we are limited to examining them through investigative modelling efforts and focus on the influence of atmospheric chemical composition.

Previous studies using general circulation models (GCMs) have shown that close-in M dwarf planets, tidally locked or otherwise, may be habitable (e.g. Boutle et al. 2017; Kopparapu et al. 2017; Turbet et al. 2017; Meadows et al. 2018). For a terrestrial planet the global circulation is driven almost entirely by stellar radiation, which is by far the largest heat source in the system. Naturally, this creates spatial inhomogeneities. For a tidally locked planet with a permanent day and nightside, these inhomogeneities are even more exaggerated. In this scenario, the three-dimensional nature of the system – a hot dayside, a cold nightside, and an atmospheric jet transporting heat and moisture around the equator – means that one-dimensional models are not necessarily sufficient to properly simulate the atmospheric dynamics. This is especially true when clouds and convection are involved, as these processes are difficult to simulate in one dimension (see e.g. Tompkins 2000; Palmer 2012, for a discussion of these difficulties). Historically, GCM studies of M dwarf planets have not incorporated an interactive chemistry scheme, partly due to the uncertainties in the atmospheric composition, partly due to the perceived sufficiency of understanding atmospheric chemistry using 1D models, and partly because of the perception that it plays an insignificant contribution to the mean climate. Informed by the results from GCMs, one might expect that the spatial inhomogeneities in the circulation and dynamics drive non-uniform chemistry, resulting in planets that have different day and nightside chemical environments (Proedrou & Hocke 2016; Drummond et al. 2018). This is relevant to tidally locked planets, which have broad Rossby gyres on the nightside (Showman & Polvani 2011) that temporarily trap air that is consequently subject to extended periods of radiative cooling, resulting in localized cold spots; extreme day–night temperature differences compared with a fast-rotating planet like Earth; and portions of the atmosphere or surface that are never exposed to stellar radiation.

Integrating atmospheric chemistry and physics into GCMs is therefore a natural next step for exoplanet science, and is relevant also for understanding and testing potential atmospheric biosignatures (Seager 2014). Spatial inhomogeneities in atmospheric biosignatures, driven by atmospheric chemistry and physics, will affect our ability to detect them (e.g. transmission geometry) and to interpret them in the absence of 3D models. In the case of habitable M dwarf planets, direct detection, where spectra are hemispherically averaged, is not likely to be possible for many years due to their associated small angular separations from their host star. Transmission and thermal phase curves therefore represent the main current observing modes for these planets, for which terminator profiles and day–night contrasts will be the most important. Conversely, the observed variations in these biosignatures, interpreted using 3D model analogues, may identify which ones are most robust.

Previous work that studied a tidally locked Earth, although orbiting the Sun in 365 d, showed significant chemical differences on the day and nightside of the planet (Proedrou & Hocke 2016). Using a simple ozone photochemistry model, they showed that ozone was present on both sides but was present in higher concentrations on the nightside. They also found that for the nightside, where chemical e-folding lifetimes are longest, atmospheric transport was most important for determining ozone distributions. This work only has limited applicability to M dwarf planets such as Proxima Centauri b. The stellar radiation spectrum plays a critical role in determining ozone chemistry. It is unclear *a priori* whether a star emitting less UV radiation than the Sun would be able to establish and sustain an ozone layer. Generally, being able to maintain a layer of radiatively active gas, such as ozone, will influence the habitability of the planet directly via the surface radiation environment and indirectly via climate feedbacks. Recent work has used the CAM-Chem 3D model to study atmospheric chemistry on M dwarfs (Chen et al. 2018). These authors also discussed the day–night differences in chemistry, and emphasized the importance of using self-consistent chemistry fields for interpreting observations. We discuss this study in the context our work later in Section 4.

In this work, we examine the sustainability of an ozone layer on a tidally locked M dwarf planet. We use a global 3D GCM that describes a terrestrial exoplanet, nominally Proxima Centauri b, building on Boutle et al. (2017). The GCM is a generalized version of the Met Office Unified Model (UM), which is used extensively for short-term weather prediction and long-term climate studies for the Earth (Walters et al. (2017). The UM has been used previously to study the atmospheric physics of terrestrial exoplanets and hot Jupiters (e.g. Mayne et al. 2014a, b; Boutle et al. 2017; Drummond et al. 2018; Lewis et al. 2018). We couple this model with the Chapman mechanism (Chapman 1930) that describes ozone chemistry in Earth's stratosphere with the hydrogen oxide catalytic cycle. The UM and the atmospheric chemistry are described in Section 2. In Section 3, we report our results that describe variations of atmospheric ozone on a tidally locked M

**Table 1.** Planetary parameters for the simulated Proxima Centauri b planet. The numbers in round brackets represent the ratio with resepect to values for Earth.

| Parameter | Value |
|---|---|
| Semimajor axis/au | 0.0485 |
| Stellar irradiance/W $m^{-2}$ | 881.7 (0.646) |
| Orbital period/Earth days | 11.186 |
| $\Omega$/rad $s^{-1}$ | $6.501 \times 10^{-6}$ |
| Eccentricity | 0 |
| Obliquity | 0 |
| Radius/km | 7160 (1.1) |
| $g$/m $s^{-1}$ | 10.9 |

dwarf planet and the responsible chemical reactions. We conclude the paper in Section 4.

## 2 MODEL DESCRIPTION

Table 1 shows an overview of the physical parameters that define the Proxima Centauri b simulation, following Boutle et al. (2017). For the sake of brevity, we focus here on key aspects of the simulation and refer the reader to Mayne et al. (2014a, b) and Boutle et al. (2017) for a comprehensive model description. We run the model at a horizontal spatial resolution of 2° (latitude) × 2.5° (longitude), with the substellar point defined at latitude and longitude 0°. We increase the upper altitude boundary of the model from 40 km (Boutle et al. 2017) to 85 km, described on 60 levels of which 38 levels describe the atmosphere from the surface to 40 km and are identical to those used by Boutle et al. (2017). We increased the model upper boundary to improve the description of ozone dynamics in the upper atmosphere. We also reduced the dynamical model time-step from 20 min, as adopted by Boutle et al. (2017), to 12 min to avoid high wind speeds above altitudes of 40 km violating the Courant–Friedrichs–Lewy condition. Chemistry and radiation time-steps were left unchanged from a default value of one hour.

Fig. 1 shows our assumed radiation spectrum for Proxima Centauri, taken from BT-Settl model library for an M dwarf with $T_{\rm eff} = 3000$ K, $g = 1000$ m $s^{-2}$, and metallicity = 0.3 dex (Rajpurohit et al. 2013). Using this spectrum, which approximately follows a blackbody distribution, allows us to directly compare our results with previous results that used fixed atmospheric composition (Boutle et al. 2017). Consequently, Proxima Centauri emits less radiation at UV wavelengths relevant to the Chapman mechanism (see photochemical reaction 2 below) than the Sun because of its lower blackbody temperature. We acknowledge that this energy distribution does not include stellar activity, so represents a quiescent star, and does not include Lyman-$\alpha$ emission. Numerical experiments by the authors (not shown) suggest that including Lyman-$\alpha$ emissions would likely result in only a small increase in total $O_3$ columns and a small corresponding change in atmospheric heating.

The UM has the capability to describe gas (Morgenstern et al. 2013; Telford et al. 2013) and aerosol phase (Mann et al. 2010) chemical mechanisms, developed collectively under the UK Chemical and Aerosol (UKCA) project, that is typically used to explore how atmospheric composition affects Earth's climate. Here, we use relatively simple ozone chemistry (described below), but the underlying infrastructure allows this work to be easily extended to study more complex organic chemistry. The atmospheric chemistry is fully 3D with advection and turbulent mixing, and chemical species are included in the radiation scheme, making the model self-consistent.

We use the Chapman mechanism (reactions R1–R4, Chapman 1930) to describe the main characteristics of atmospheric ozone on our tidally locked M dwarf. This mechanism forms the basis of our understanding of observed variations in stratospheric ozone. However, the mechanism overpredicts stratospheric ozone on Earth mainly because it does not take into account catalytic cycles. The mechanism is initiated in R1 by the photolysis of molecular oxygen by high-energy UV photons ($\lambda < 240$ nm), producing atomic oxygen in the ground-level triplet state $O(^3P)$, denoted here as O, which are highly reactive and combine rapidly with $O_2$ to form ozone (R2). $H$ denotes an inert molecule such as $N_2$ or $O_2$ that dissipates the energy associated with the reaction. The resulting ozone molecules can be photolyzed (R3) at longer wavelengths (less energetic photons, $\lambda < 320$ nm) to produce O in its excited singlet state $O(^1D)$ that is rapidly stabilized to $O(^3P)$ by collision with $N_2$ or $O_2$. R4 describe the slow loss of ozone due to reaction with atomic oxygen.

$$O_2 + h\nu \rightarrow O + O(\lambda < 240\,\text{nm}) \quad \text{(R1)}$$
$$O + O_2 + H \rightarrow O_3 + H \quad \text{(R2)}$$
$$O_3 + h\nu \rightarrow O_2 + O(\lambda < 320\,\text{nm}) \quad \text{(R3)}$$
$$O_3 + O \rightarrow O_2 + O_2 \quad \text{(R4)}$$

We include the $HO_x$ (sum of the hydroxyl radical OH and hydroperoxy radical $HO_2$) catalytic cycle (Roney 1965), acknowledging that our atmosphere also includes water vapour that can lead to ozone loss.

$$H_2O + O(^1D) \rightarrow 2OH \quad \text{(R5)}$$
$$OH + O_3 \rightarrow HO_2 + O_2 \quad \text{(R6)}$$
$$HO_2 + O_3 \rightarrow OH + 2O_2 \quad \text{(R7)}$$
$$\textbf{Termination}: \quad OH + HO_2 \rightarrow H_2O + O_2 \quad \text{(R8)}$$

The catalytic cycle comprises of an initiation step (R5), propagation steps that destroy ozone and recycle the catalysis (R6 and R7), and a termination step that represents a loss of the catalysis (R8). We also retain values used by UKCA for ozone dry deposition, which represents a minor loss terms except near the planetary surface. We describe dry deposition of ozone over water following Giannakopoulos et al. (1999), using a value of 0.05 cm $s^{-1}$ (Ganzeveld & Lelieveld 1995).

We define our initial conditions using an Earth-like configuration, comprised of $N_2$ (approximately 77 per cent), 23.14 per cent $O_2$ (mass mixing ratio, MMR), and 0.0594 per cent $CO_2$ (MMR), with the remainder being composed of ozone chemistry tracers that we describe above. We do not consider $CH_4$ and $N_2O$ in our atmosphere because these trace gases imply life and significantly complicate our chemical mechanism, but they are included in Boutle et al. (2017). With the exception of $N_2$, $CO_2$, $O_2$, and $H_2O$, we set the other gases associated with chemistry to a uniformly distributed MMR value of $10^{-9}$ to minimize the influence of initial conditions on subsequent model fields; $H_2O$ is calculated based on evaporation from the slab ocean. We spin-up the model fields for 20 yr from those initial conditions. We find that the atmospheric ozone state reaches a quasi-equilibrium after 5–10 yr subject to stochastic changes in atmospheric dynamics. As a conservative approach, the results we present here are a mean of 120 d that immediately follow the 20-yr spin-up period. We perform three model runs: a calculation including the Chapman $O_3$ mechanism with and without

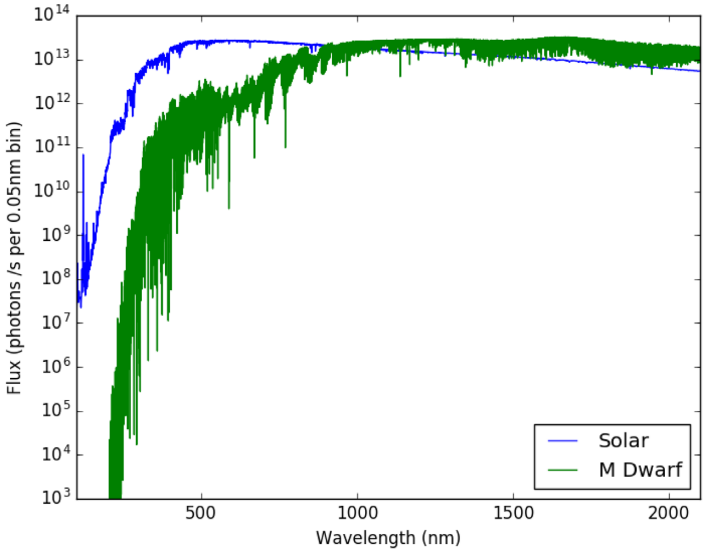


**Figure 1.** Top-of-the-atmosphere fluxes (photons/s/0.05 nm bin) as a function of wavelength (nm) for Proxima Centauri b (green) and Earth (blue), both scaled to the semimajor axis of orbit.

**Table 2.** M dwarf top-of-atmosphere (TOA) fluxes at spectral bands used by the UKCA model, reported at 1 au.

| Wavelength band (nm) | TOA flux at 1 au (photons $s^{-1}$ $cm^{-2}$) |
|---|---|
| 187 | 2.213 |
| 191 | 2.874 |
| 193 | 3.589 |
| 196 | $1.205 \times 10^{1}$ |
| 202 | $3.502 \times 10^{1}$ |
| 208 | $5.388 \times 10^{2}$ |
| 211 | $6.885 \times 10^{2}$ |
| 214 | $1.684 \times 10^{5}$ |
| 261 | $2.107 \times 10^{7}$ |
| 267 | $4.660 \times 10^{7}$ |
| 277 | $1.922 \times 10^{8}$ |
| 295 | $9.886 \times 10^{8}$ |
| 303 | $1.066 \times 10^{9}$ |
| 310 | $3.349 \times 10^{9}$ |
| 316 | $1.390 \times 10^{10}$ |
| 333 | $1.110 \times 10^{11}$ |
| 380 | $1.980 \times 10^{12}$ |
| 574 | $1.319 \times 10^{15}$ |

the $HO_x$ catalytic cycle, and a model run using a fixed Earth-like $O_3$ distribution, following Boutle et al. (2017).

We use two separate but consistent radiation schemes in the model. The SOCRATES radiative transfer model describes the radiation processes in the physical model using six short-wave and nine long-wave bands (Edwards & Slingo 1996; Manners et al. 2015), and represents the default UM radiation scheme. The chemistry module uses a separate radiation scheme, Fast-JX Wild (Zhu & Prather 2000; Telford et al. 2013), that is spectrally resolved into 18 bands (Table 2) corresponding to atmospheric chemistry.

## 3 RESULTS

Here, we report results from our numerical experiments that follow our 20-yr spin-up period, as described above. Reported values represent a 120-d mean. We focus our attention on ozone chemistry from our control run, referring the reader to Boutle et al. (2017) for a detailed discussion on the corresponding atmospheric physics and climate. Sensitivity runs will be discussed explicitly with reference to the control run.

### 3.1 Hemispheric mean 1D meteorological and ozone structure

Fig. 2 summarizes the physical and chemical systems associated with our control run that includes the reactive ozone chemistry, described by reactions R1–R8. Below an altitude of 10 kilometres there are a number of differences between the day and nightsides of the tidally locked planet, as expected. Compared to the nightside, the dayside wind speeds are $\simeq$20 m $s^{-1}$ slower, specific humidity is much higher and increases towards the surface, UV is non-zero and falls off steadily as a function of depth associated with cloud cover and ozone chemistry. The small, non-zero amount of humidity on the nightside reflects transport from the dayside near the terminator. Temperature is approximately constant from an altitude of 2 km towards the surface on the dayside, while there is a strong negative gradient on the nightside over the same altitude range. Above 10 km, there is little difference between the distribution and values of air temperature and wind speed, suggesting an efficient transport of heat between the hemispheres (Yang & Abbot 2014; Lewis et al. 2018). There is a strong peak in wind speed between 20 and 30 km, reflecting a jet stream structure. This is in broad agreement with Boutle et al. (2017).

Fig. 2 also shows that ozone is vertically distributed, peaking between 20 and 30 km; this is similar to the structure we find in Earth's atmosphere. This peak in ozone is slightly broader on the nightside, reflecting the presence of cold traps that result in a local build-up of ozone. R1 and R4 describe the production and loss of ozone. On the dayside there is a large production rate due to the photolysis of $O_2$ throughout the atmosphere, falling off towards the surface due to clouds; this reflects the penetration of UV through the atmosphere. The production rate is much smaller for the nightside, with non-zero values due to transport from the dayside. The dayside loss rate (R4) is highest above 10 km, some 90 per cent smaller

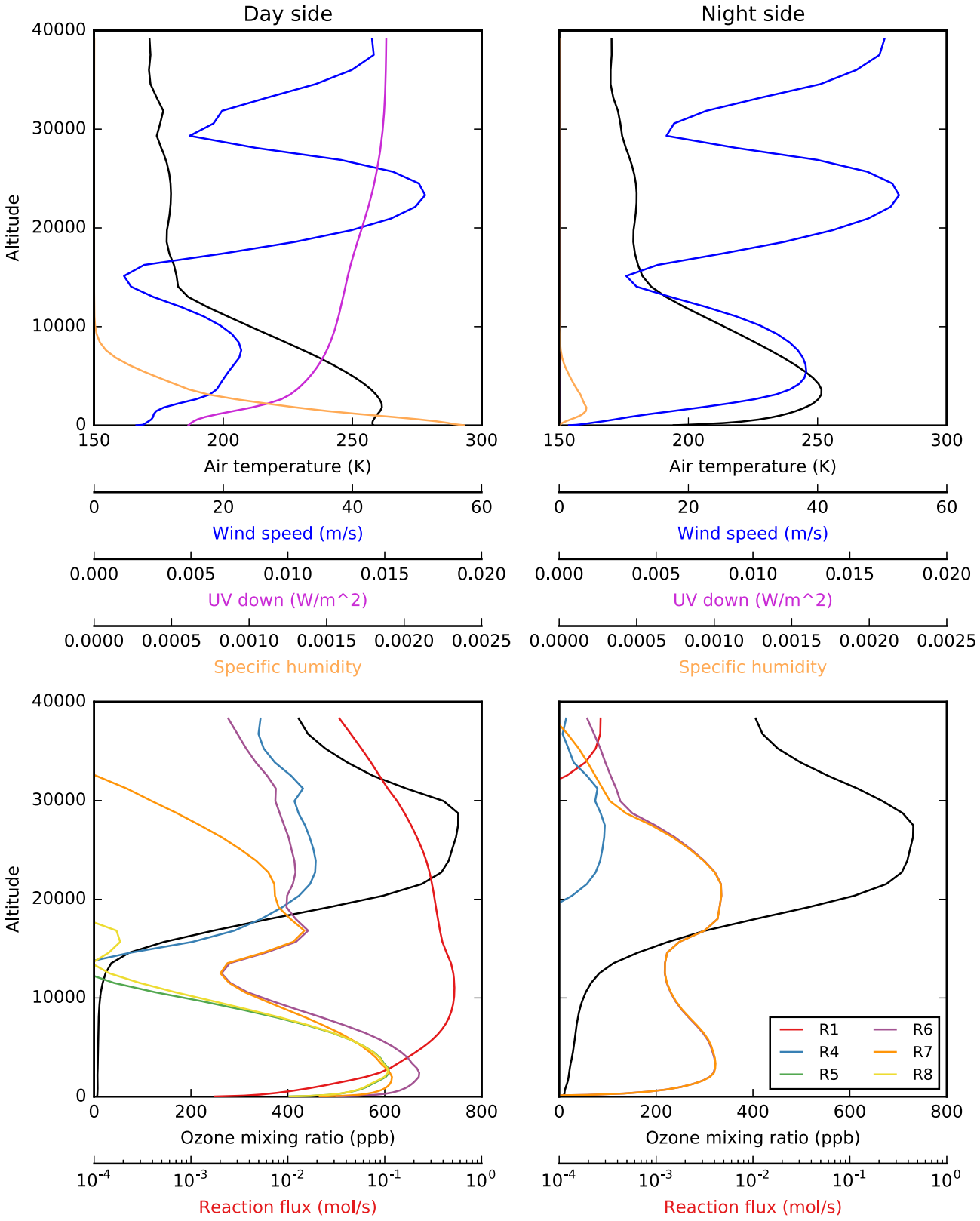


**Figure 2.** (Left-hand panels) Dayside and (Right-hand panel) nightside hemispheric means of (top panels) meteorological and (bottom panels) chemical parameters on a tidally locked M dwarf planet. The values correspond to a 120-d mean immediately succeeding a 20-yr spin-up period. The black lines in the bottom panels show ozone concentration (ppb) per model grid box and the coloured lines show the corresponding reaction fluxes (mol $s^{-1}$), which are plotted on a logarithmic scale as flux per model grid box.

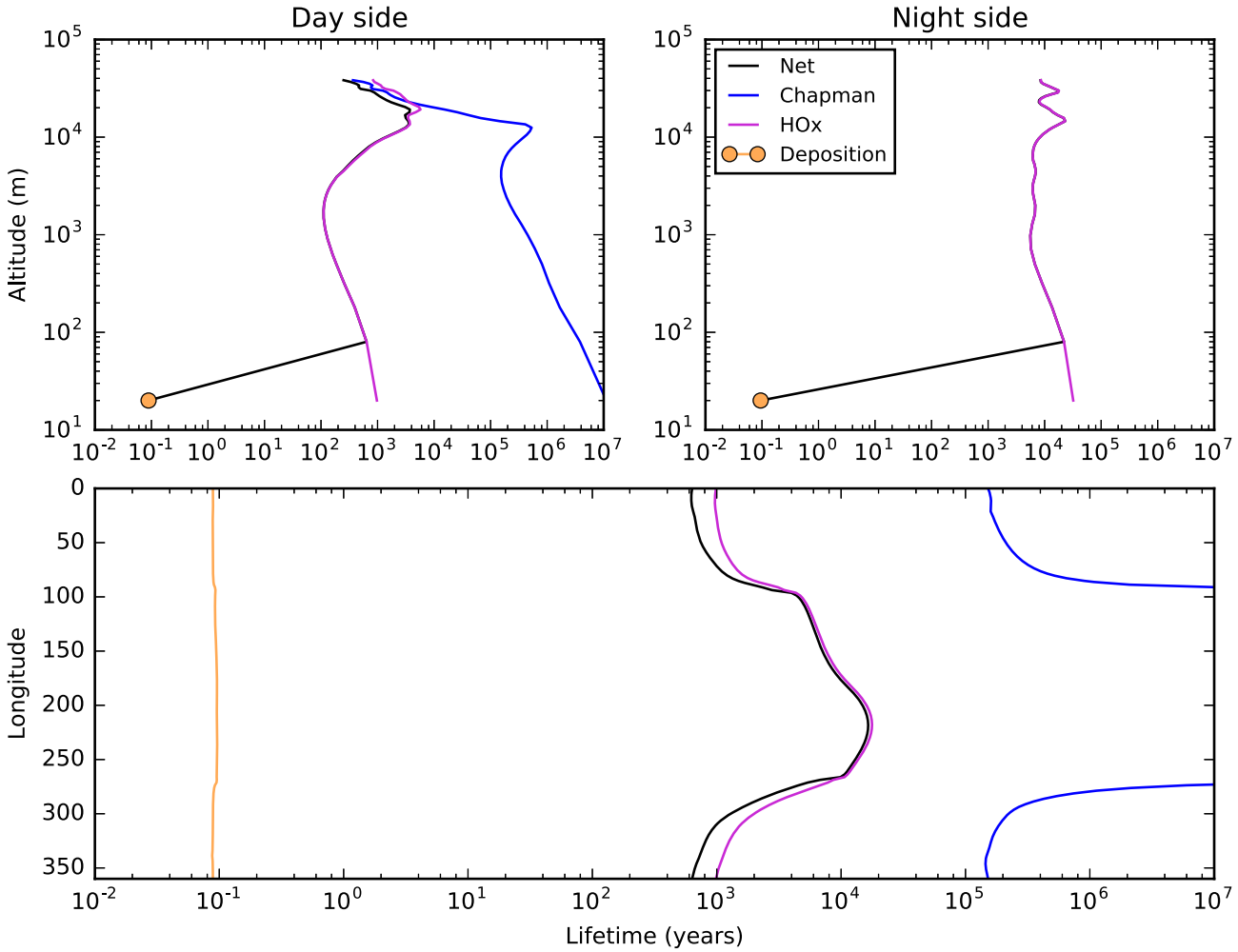


**Figure 3.** The total and contributing atmospheric lifetimes on a tidally locked M dwarf planet, expressed in years, of atmospheric ozone against chemistry and deposition on the (left-hand panel) dayside and (right-hand panel) nightside hemispheres. The bottom panel describes atmospheric lifetime as a function of longitude (mean taken over latitude and altitude) encompassing both hemispheres. The contributing lifetimes denoted as Chapman and $HO_x$ denote the lifetime of ozone against R4 and against the $HO_x$ catalytic cycle, respectively. The values correspond to a 120-d mean immediately succeeding a 20-yr spin-up period.

than the production rate. The corresponding nightside loss rate is much smaller, mainly due to the absence of $O(^1D)$ produced by the photolysis of $O_3$. Below 10 km, the dominant loss rates are due to the $HO_x$ catalytic cycle, with a vertical distribution following the abundance of atmospheric humidity, as expected. On the nightside, $HO_x$ radicals are exclusively transported from the dayside, where the associated *in situ* initiation step R5 and the termination step R8 are extremely small (Fig. 2).

Fig. 3 shows the lifetime of atmospheric ozone against the Chapman loss term, the $HO_x$ catalytic cycle, and from deposition. We also show the mean net ozone lifetime corresponding to the action of these three loss processes. This lifetime is of the order of hundreds of years, increasing to 10 000 yr when ozone is trapped in the nightside cold traps, described below, with a sharp increase in ozone lifetime at the terminators that reflects a rapid decrease in UV radiation necessary to generate atomic oxygen (R1). We find that the loss due to the $HO_x$ catalytic cycle largely determines the net atmospheric lifetime of ozone on the day and nightsides of the planet. The only exception is near the surface where the deposition loss process dominates. The atmospheric lifetime of ozone is an order-of-magnitude longer on the nightside of the planet, as expected, due to the absence of photons. Atmospheric transport and diffusion processes are orders of magnitude faster than loss processes due to chemistry. The corresponding residence times (non-chemistry lifetimes) typically range 0.1–10 h in a grid box, and occasionally 100 h in the laminae layers of low-wind speed that lie between the jet streams, as discussed below.

### 3.2 3D ozone structure

Here, we focus on the 3D structure of atmospheric ozone and its precursors, and refer the reader to Appendix A (online) for the associated meteorological fields.

Fig. 4 shows the 3D distribution of atmospheric ozone. We also show integrated column amounts of ozone, expressed in Dobson units (DU) that are commonly used to report ozone in Earth's atmosphere. One DU is defined as the thickness (in units of 10 microns) of the layer of a pure gas that would be formed by the integrated column amount at standard temperature and pressure, equivalent to $2.69 \times 10^{20}$ molec cm$^{-2}$. Ozone columns are largest on the nightside, localized within two Rossby gyres either side of an approximately uniform equatorial band that corresponds to the rapid transport of air in the equatorial zonal jet (Showman & Polvani 2011). The cyclonic gyres effectively trap air

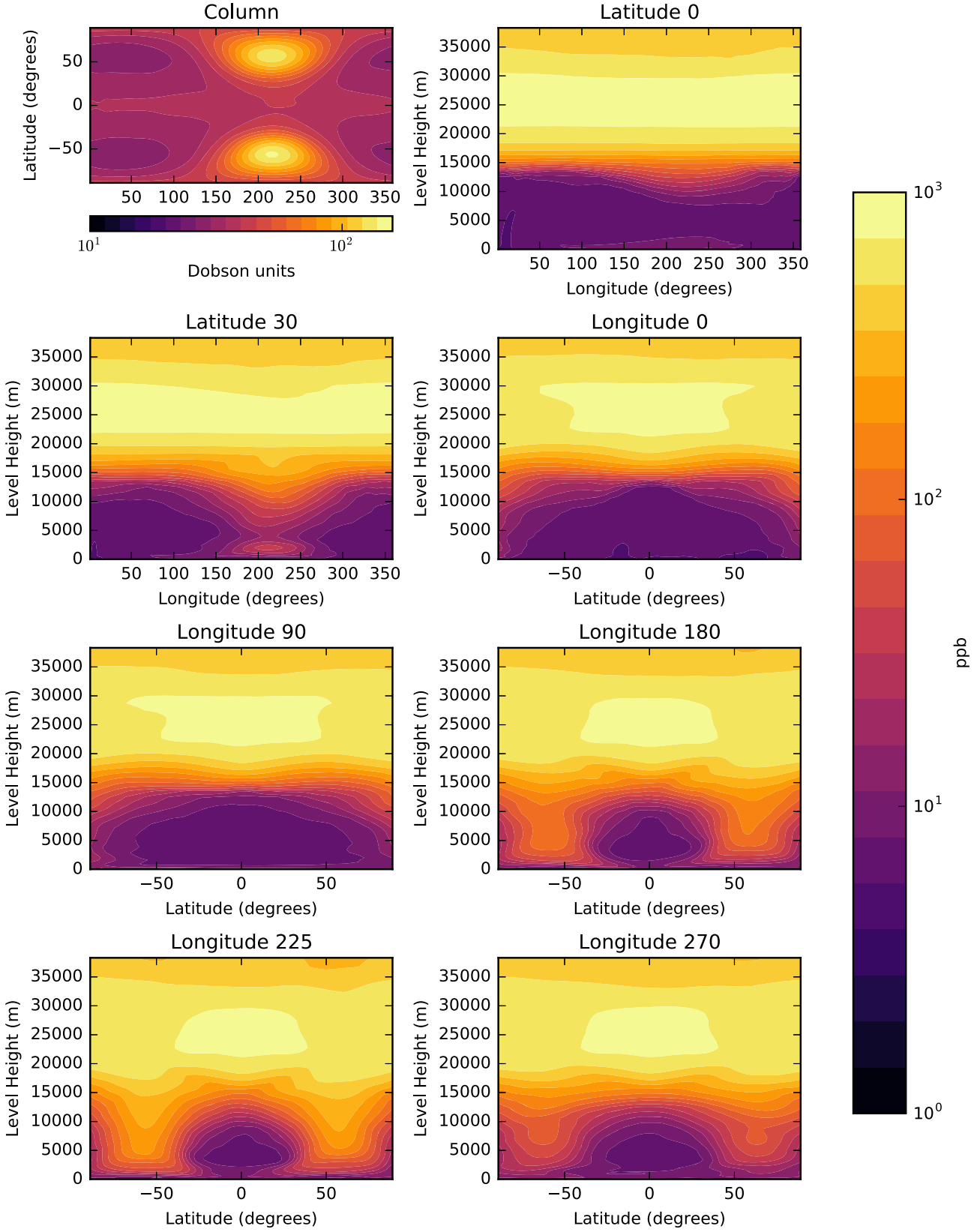


**Figure 4.** Atmospheric ozone distributions on a tidally locked M dwarf planet. The values correspond to a 120-d mean immediately succeeding a 20-yr spin-up period. The top left panel shows $O_3$ columns in Dobson units (DU), where one DU is equivalent to a layer of ozone that is 0.01 mm thick at standard temperature and pressure. The remaining panels show meridional or zonal slices that correspond to latitudes and longitudes, respectively, across the planet.

that subsequently experience extended periods of radiative cooling, resulting in localized columns of cold air. Within these cold traps the atmosphere partially collapses (Fig. 4, longitude 225°) so that large values of ozone, typical of the higher atmosphere, are brought down to lower altitudes, resulting in higher ozone columns. On the dayside, ozone columns are largest at the poles. The smallest ozone columns (≃30 DU) are found the dayside at northern and southern mid-latitudes. Column ozone values on our M dwarf planet are typically an order-of-magnitude smaller than those found on Earth (≃300 DU) with the exception of the interior of the nightside Rossby gyres, where ozone is 140 DU.

Fig. 4 also shows atmospheric mole fractions of ozone are at a minimum on the dayside near the substellar point. This corresponds to the location of the maximum ozone production and loss rates (R1 and R4), Figs 5 and 6, driven by the availability of incoming UV radiation. The fast exchange between O and ozone, R2 and R3 (Figs 7 and 8, respectively), results in reaction fluxes that are up to five orders of magnitudes larger than that the Chapman production (R1) and loss (R4) fluxes of ozone and peaking on the dayside. In the absence of UV radiation, nightside ozone mole fractions are determined mostly by atmospheric transport but also by the comparatively slow $HO_x$ catalytic cycle loss process. We find that e-folding chemical lifetimes of ozone (Fig. SB3) within any grid box are much longer than the residence time for an airmass to pass through the same grid box (Fig. SB4). Initiation of the $HO_x$ catalytic cycle (R5) happens only on the dayside, where warmer atmospheric temperatures permit atmospheric humidity, but the propagation reactions R6 and R7 (Figs SB1 and SB2) continue on the nightside.

To understand the impact of our assumed ozone chemistry mechanism on the climate of Proxima Centauri b, we present model results from a sensitivity run that uses an alternative fixed distribution of Earth-like (larger) ozone that ranges from $2.4 \times 10^{-8}$ to $1.6 \times 10^{-5}$ MMR with the largest values in the stratosphere (Boutle et al. 2017). We denote this run as 'No chem'. We also consider a model run ('No HOx') in which we remove the $HO_x$ ozone catalytic cycle (reactions R5–R8). Fig. 9 shows the mean hemispheric dayside and nightside values of the sensitivity minus control runs. On the dayside, 'No-chem' ozone results in 5 K warmer and 5 K cooler temperatures above and below 15 km, respectively. The increased temperatures correspond to the altitude of peak ozone due to ozone absorption and heating. On a hemispheric scale, atmospheric ozone reduces the amount of incoming radiation penetrating through the atmosphere, with the largest reductions at the substellar point, thereby cooling altitudes below. Larger Earth-like ozone values result in a near-surface cooling of 2.6 K. We find a similar situation on the nightside, except that near-surface temperatures are 4 K warmer, due to faster movement of dayside polar air to mid-latitudes on the nightside. These warmer nightside temperatures are accompanied by higher levels of specific humidity below 10 km. Removing the $HO_x$ catalytic cycle from the interactive chemistry scheme generally has a smaller impact on atmospheric physics than adopting a fixed Earth-like ozone distribution. The catalytic cycle is most important in the upper atmosphere of the substellar point. Fig. 9 also show dayside surface UV zonal and meridional mean distributions, which directly reflect the differences between the control and sensitivity ozone distributions.

## 4 DISCUSSION AND CONCLUDING REMARKS

We use the Met Office UM to explore the potential of a tidally locked M dwarf planet, nominally Proxima Centauri b irradiated by a quiescent version of its host star, to sustain an atmospheric ozone layer. We have built on previous work (Boutle et al. 2017) by including the Chapman ozone photochemistry mechanism. We have also included the hydrogen oxide ($HO_x$, describing the sum of OH and $HO_2$) catalytic cycle to account for atmospheric water vapour that plays a role in determining the distribution of atmospheric ozone. We find that the host M dwarf star radiates with sufficient energy at UV wavelengths to initiate and sustain an ozone layer on Proxima Centauri b. The quasi-stationary atmospheric distribution of atmospheric ozone is determined by photolysis driven by incoming stellar radiation and by atmospheric transport. Ozone production rates, determined by the photolysis of molecular oxygen, and loss rates, determined by reaction between ozone and excited atomic oxygen, are largest near the substellar point, as expected. Reaction fluxes involving photolysis get progressively smaller towards the terminators, as expected. Concurrently, excited atomic oxygen is quenched by molecular oxygen to rapidly form ozone, resulting in large ozone concentrations on the nightside of the planet. We find the ozone mole fractions are smallest (largest) in the lowest 15 km of the atmosphere at the (anti) substellar point. Above 15 km the ozone distribution is dominated by an equatorial jet stream that rapidly moves ozone around the planet. The nightside ozone distribution is dominated by two Rossby gyres that leads to prolonged radiative cooling of trapped air, resulting in a localized collapse of the atmosphere that brings down higher ozone values to the lower atmosphere.

The calculations we report here are valid for a quiescent version of the host star. Preliminary calculations (not shown) that crudely describe a stellar electromagnetic flare as a large (150 per cent–600 per cent) and a short (1 h to 1 d) perturbation to the quiescent stellar flux received at the top of our unmagnetized planetary atmosphere (Fig. 1) show that the ozone layer is resilient. The larger flux of high-energy photons on the dayside titrates $O_2$ (R1) and low-energy photons titrate $O_3$ (R3) but can regenerate using products from elevated photolysis fluxes and from reactions active on the nightside. This is qualitatively consistent with 1D calculations (Segura et al. 2010). More recent 1D calculations (Tilley et al. 2019) report that if an electromagnetic flare is accompanied by a proton ionization event, ozone can be permanently removed from the atmosphere. The extent of this ozone removal is driven by the magnitude, frequency, and duration of the stellar activity.

We find the planetary surface is potentially habitable in our calculations, in agreement with Boutle et al. (2017), with a significant surface area with temperatures above 273 K. We did not consider ice-albedo feedback, following Shields et al. (2013), Boutle et al. (2017), and Lewis et al. (2018) who showed this effect is small for M dwarf planets. For our planetary calculations we adopted Earth-like $CO_2$ concentrations, but we acknowledge they are likely too low if there exists a carbonate–silicate negative feedback cycle (Walker, Hays & Kasting 1981). This feedback mechanism has the potential to increase the geographical region with surface temperatures above 273 K, depending on a number of factors, e.g. surface geology and tectonic activity.

We show that the thin ozone layer (tens of Dobson units) on the dayside, supported by incoming UV radiation, is sufficient to reduce the incoming UV by 60 per cent from 40 to 0 km, as inferred by reduced photolytic production rates of excited atomic oxygen as a function of atmospheric depth. Previous studies that used a 1D model found similar results (e.g. O'Malley-James & Kaltenegger 2017). Near-surface warming results in water cloud formation that further reduces the UV penetration in the atmosphere. Surface ozone

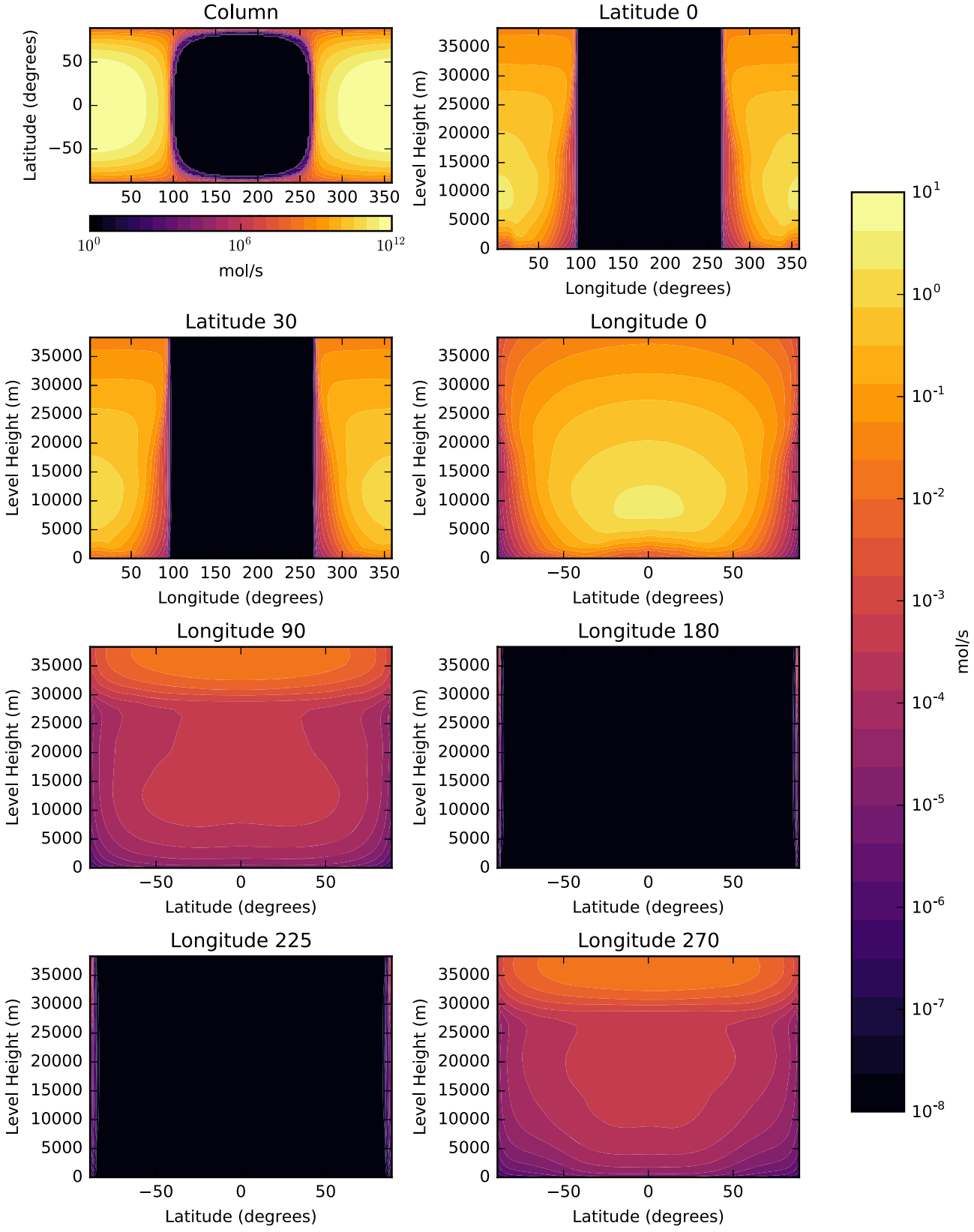


**Figure 5.** Reaction flux (mol $s^{-1}$) $O_2 + h\nu \rightarrow O + O$ (reaction R1) corresponding to atmospheric ozone distributions on a tidally locked M dwarf planet. The values correspond to a 120-d mean immediately succeeding a 20-yr spin-up period. The format of the plot corresponds to Fig. 4.

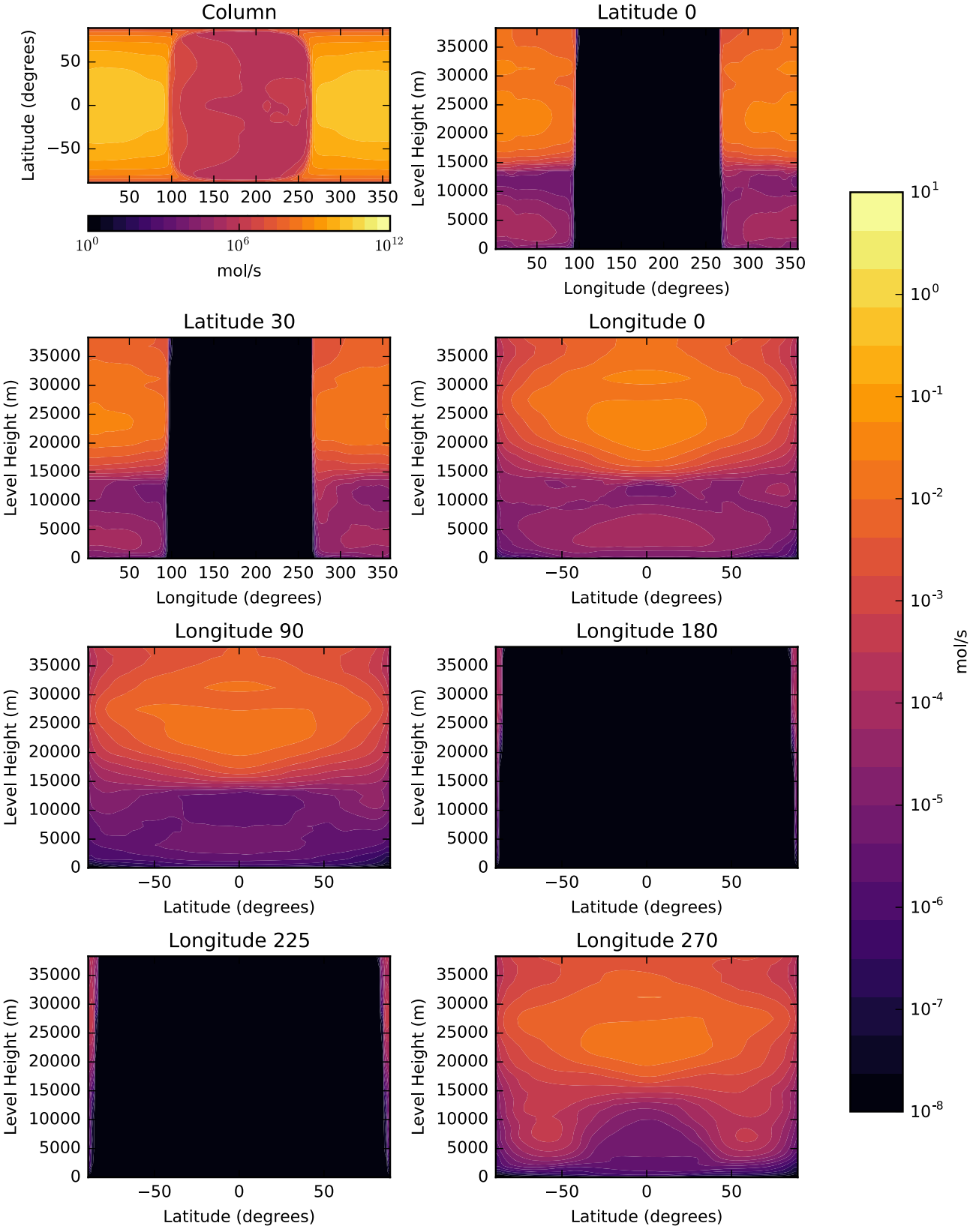


**Figure 6.** As Fig. 5 but for reaction flux (mol $s^{-1}$) $O_3 + O \rightarrow 2O_2$ (reaction R4).

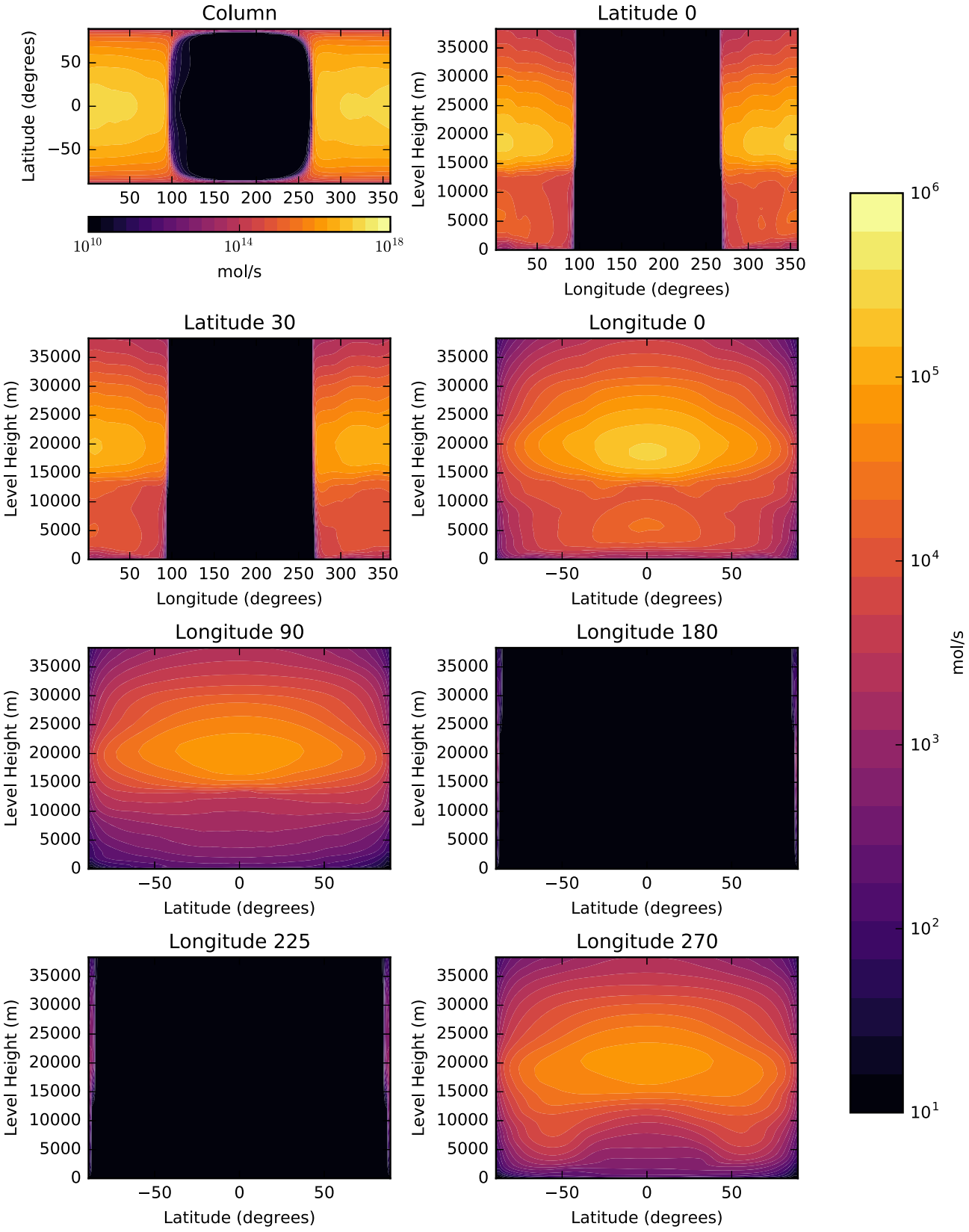


**Figure 7.** As Fig. 5 but for reaction flux (mol $s^{-1}$) $O + O_2 + H \rightarrow O_3 + H$ (reaction R2).

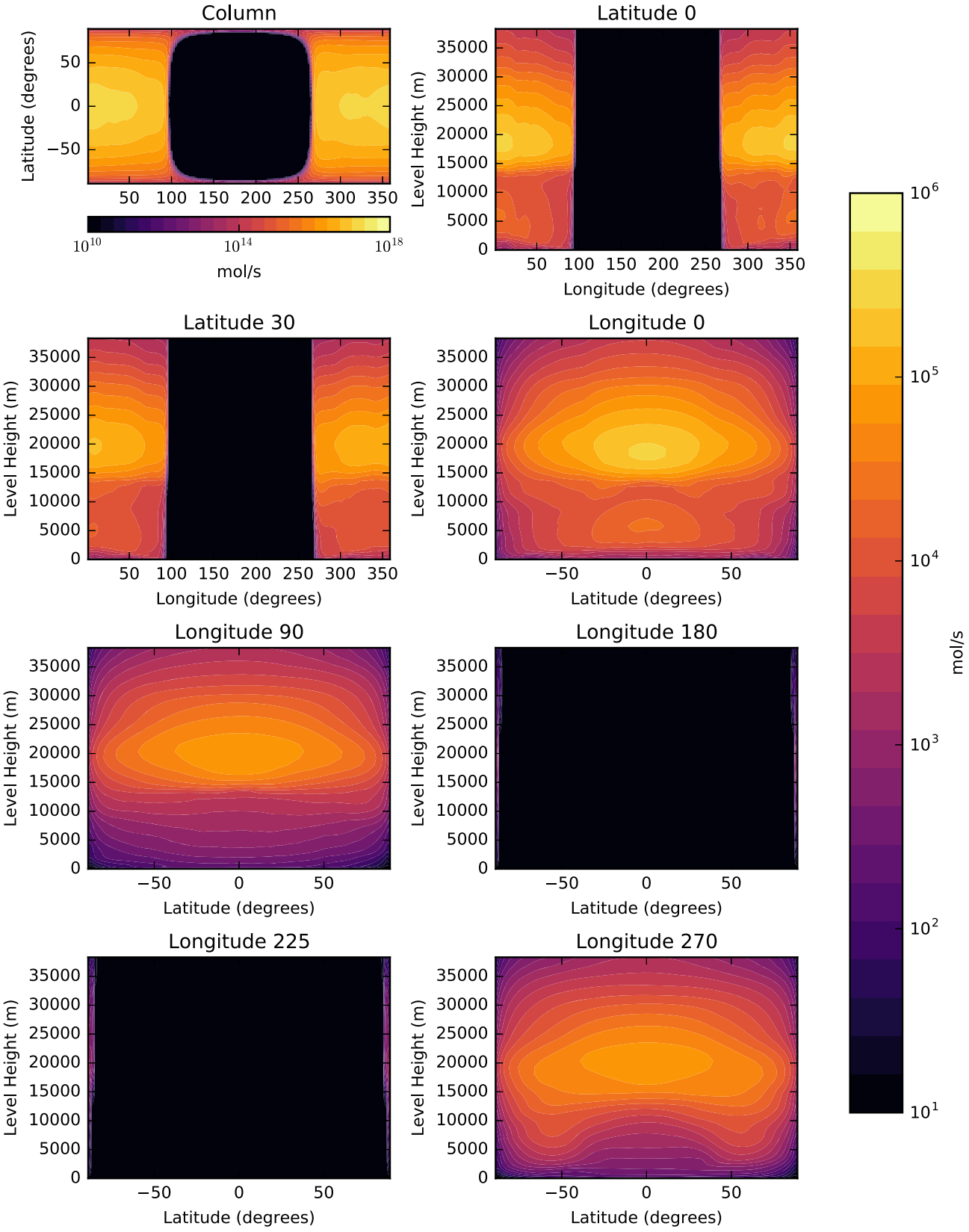


**Figure 8.** As Fig. 5 but for reaction flux (mol $s^{-1}$) $O_3 + h\nu \rightarrow O_2 + O$ (reaction R3).

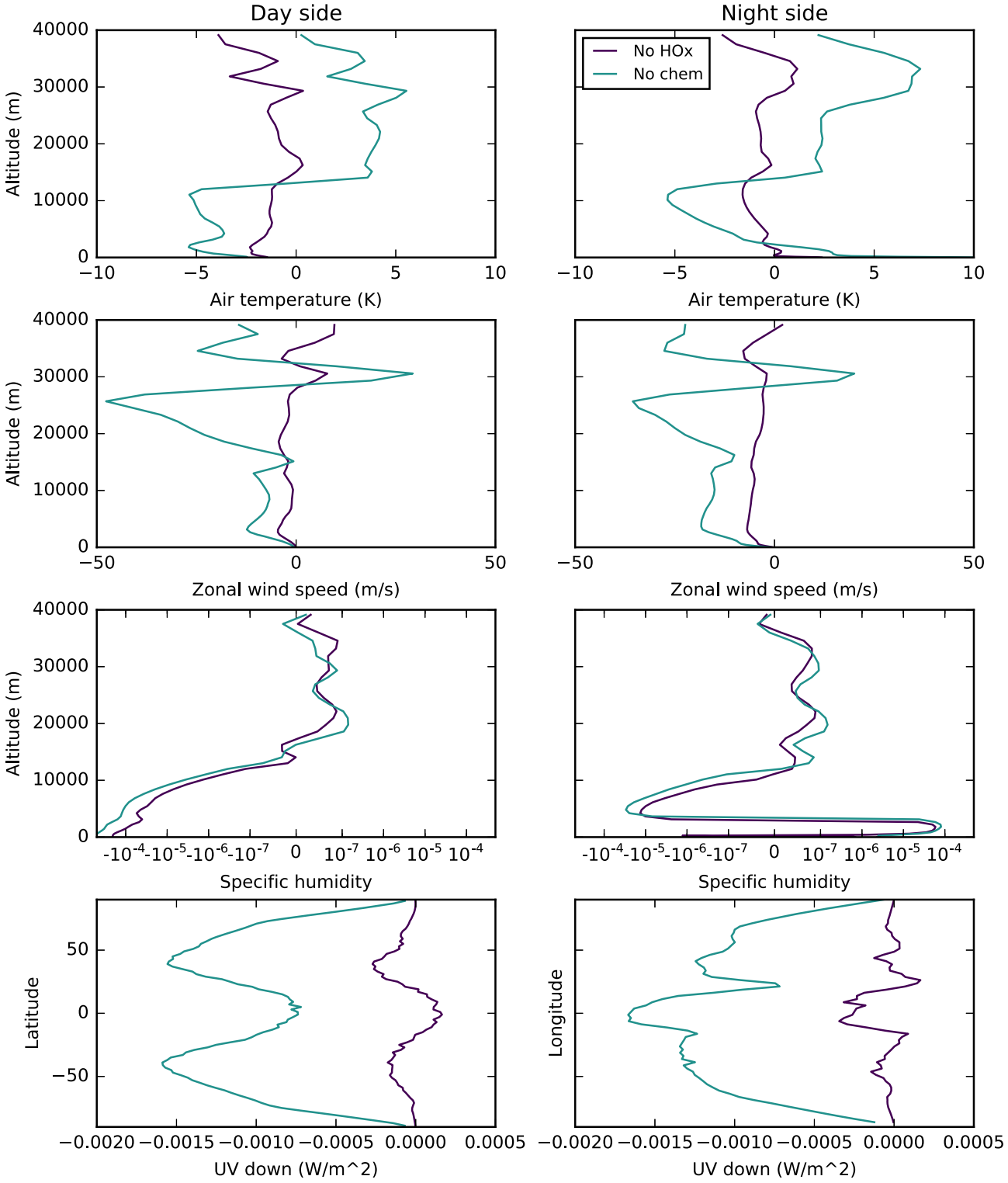


**Figure 9.** Sensitivity minus control differences of key meteorological parameters on a tidally locked M dwarf planet that includes atmospheric ozone chemistry. The control calculation describes interactive ozone chemistry, described by the Chapman mechanism and the $HO_x$ catalytic cycle, that is consistent with the physical environment. The two sensitivity runs are (1) No-Chem, which uses a static Earth-like 3D ozone distribution; and (2) No $HO_x$, which describes the interactive ozone chemistry but without the catalytic cycle. The top three panels describe (left) dayside and (right) nightside hemispheric mean values. For the specific humidity plot, the abscissa is symmetric about zero: linear between $-10^{-7}$ and $10^{-7}$, with the remainder described on a logarithmic scale. The bottom panels show zonal and meridional mean surface UV for the planet dayside.

levels are typically lower than 9 ppb, far below values that are associated with values that trigger human respiratory illnesses and crop damage.

A previous study (Chen et al. 2018) that comes the closest to our experiments is sufficiently different to permit only a qualitative comparison. That study uses the CAM-Chem 3D model for Earth with an atmospheric chemistry scheme described by 97 species and 196 reactions, in comparison with our model with a reduced description of ozone chemistry. The CAM-Chem model describes atmospheric dynamics using 26 levels (surface–50 km) while our model uses 60 levels (surface–80 km), allowing us to explore in more detail the general circulation. They used stellar insolation of 1360 $W\,m^{-2}$ while we used 881.7 $W\,m^2$, and our stellar spectrum contained less UV radiation that even their quiescent M dwarf. Finally, Chen et al. (2018) used Earth continents as part of their surface boundary conditions including a prescribe land/ice scheme, while we use a shallow water world without continents or prescribed ice. Lewis et al. (2018) showed that continents can significantly affect the climate of tidally locked planets via convection and evaporation of water, but acknowledge that Chen et al. (2018) placed their substellar point in the middle of the Pacific Ocean where there are no large land masses. Despite these many differences between the two experiments, our findings are broadly similar. In particular, the contrast between ozone on day and nightsides is mainly determined by variations in UV radiation, and corresponding changes in ozone lifetime, and the tidal locking of the planet results increases the inhomogeneity of ozone. Both studies also find that transported $HO_x$ species are an important sink of nightside ozone and the developing of a nightside temperature inversion. However, there are some key differences in ozone (compare their fig. 3 and our Fig. 2) that shows our ozone layer is much thinner than theirs, with our layer thinning rapidly above 30 km while theirs extends above 48 km. It is also unclear if their experiment results in the cold trap ozone accumulation, which is a prominent nightside feature. These differences are likely due to the stellar spectral energy distributions used and the role of continental orography affecting the atmospheric dynamics.

A growing body of work has promoted the use of ozone as a potential biosignature (Schwieterman et al. 2018 and references therein). In our work, we have shown that atmospheric ozone concentrations on a tidally locked planet exhibit significant spatial variations across the dayside hemisphere and between the dayside and nightside hemispheres. This illustrates the need to model planetary atmospheres in 3D to more accurately reproduce atmospheric limb or disc-averaged spectral measurements. The rapid ozone spatial variations we show at the terminators, in particular, are relevant to transmission spectroscopy along the atmospheric limb. A similar-sized planet in a different orbit around a star, e.g. 3:2 resonance orbit, may very well also exhibit strong temporal variations in ozone, reinforcing the need to (a) use 3D models to describe ozone and other reactive chemistry and (b) observe the same objects repeatedly. We anticipate a more realistic 3D distribution of atmospheric constituents will help reduce the probability of false positives and false negatives.

Our study has brought together researchers from Earth sciences and astrophysics to improve understanding of exoplanetary atmospheres. We have used a world-leading Earth system model that has been generalized for exoplanets, providing us with a flexible numerical and scientific framework on which to develop the physical, chemical, and potentially biological processes necessary to understand the habitability of individual exoplanets within the context of observational constraints. Our work here has focused on the Chapman ozone mechanism and a catalytic cycle associated with water vapour. Competing catalytic cycles operate in Earth's atmosphere, some of which are relevant to exoplanets. The nitrogen oxide catalytic cycle, initiated through emission of $NO_x$ (biogenically or through geological processes) or the thermal decomposition of $N_2$, can also lead to efficient destruction of ozone. Lightning is one such process that could achieve the necessary temperatures for thermal decomposition. More generally, processes associated with a charged atmosphere can significantly impact the physical and chemical state of the neutral atmosphere.

More broadly, we have shown that including a realistic description of radiatively active atmospheric gases that is consistent with the physical system significantly alters the physical state. Changing atmospheric heating rates via absorption of incoming and outgoing radiation alters a planet's ability to maintain liquid water at the surface and therefore being considered habitable from an anthropic perspective. Similarly, atmospheric particles lofted by aeolian processes or from the condensation of non-volatile gases can scatter and absorb incoming and outgoing radiation. To understand the habitability of exoplanets, we have to understand their atmospheric composition that can only be achieved through self-consistent global 3D models of atmospheric physics and chemistry.

## ACKNOWLEDGEMENTS

JSY was supported by the U.K. Natural Environment Research Council (Grant NE/L002558/1) through the University of Edinburgh's E3 Doctoral Training Partnership. PIP gratefully acknowledges his Royal Society Wolfson Research Merit Award. We acknowledge Adam Showman for various discussions and Paul Earnshaw who originally developed the slab ocean model used in this simulation. Materials produced using Met Office Software. JM and IAB acknowledge the support of a Met Office Academic Partnership secondment. We acknowledge use of the MONSooN2 system, a collaborative facility supplied under the Joint Weather and Climate Research Programme, a strategic partnership between the Met Office and the Natural Environment Research Council. NJM is partly supported by a Science and Technology Facilities Council Consolidated Grant (ST/R000395/1), and a Leverhulme Trust Research Project Grant.

## REFERENCES

Anglada-Escudé G. et al., 2016, Nature, 536, 437
Bochanski J. J., Hawley S. L., Covey K. R., West A. A., Reid I. N., Golimowski D. A., Ivezic Z., 2010, AJ, 2679
Borucki W. J., 2016, Rep. Prog. Phys., 79, 036901
Boutle I. A., Mayne N. J., Drummond B., Manners J., Goyal J., Hugo Lambert F., Acreman D. M., Earnshaw P. D., 2017, A&A, 601, A120
Chapman S., 1930, Mem. R. Meteorol. Soc., III, 103
Charbonneau D., Brown T. M., Noyes R. W., Gilliland R. L., 2002, ApJ, 568, 377
Chen H., Wolf E. T., Kopparapu R., Domagal-Goldman S., Horton D. E., 2018, ApJ, 868, L6
Drummond B. et al., 2018, ApJ, 855, L31
Edwards J. M., Slingo A., 1996, Q. J. R. Meteorol. Soc., 122, 689
Ganzeveld L., Lelieveld J., 1995, J. Geophys. Res. Atmos., 100, 20999
Giannakopoulos C., Chipperfield M. P., Law K. S., Pyle J. A., 1999, J. Geophys. Res. Atmos., 104, 23761
Gillon M. et al., 2017, Nature, 542, 456
Kasting J. F., 1988, Icarus, 74, 472

Kasting J. F., Whitmire D. P., Reynolds R. T., 1993, Icarus, 101, 108
Kopparapu R. K., Wolf E. T., Arney G., Batalha N. E., Haqq-Misra J., Grimm S. L., Heng K., 2017, ApJ, 845, 5
Lagrange A.-M. et al., 2010, Science, 329, 57
Léger A. et al., 2009, A&A, 506, 287
Lewis N. T., Lambert F. H., Boutle I. A., Mayne N. J., Manners J., Acreman D. M., 2018, ApJ, 854, 171
Manners J., Edwards J. M., Hill P., Thelen J.-C., 2015, Technical report, SOCRATES (Suite Of Community RAdiative Transfer codes based on Edwards and Slingo) Technical Guide. Met Office, UK
Mann G. W., Carslaw K. S., Spracklen D. V., Ridley D. A., Manktelow P. T., Chipperfield M. P., Pickering S. J., Johnson C. E., 2010, Geosci. Model Dev., 3, 519
Mayne N. J., Baraffe I., Acreman D. M., Smith C., Wood N., Amundsen D. S., Thuburn J., Jackson D. R., 2014a, Geosci. Model Dev., 7, 3059
Mayne N. J. et al., 2014b, A&A, 561, 1
Mayor M., Queloz D., 1995, Nature, 378, 355
Meadows V. S., Barnes R. K., 2018, Handbook of Exoplanets. Springer International Publishing, Cham, p. 1
Meadows V. S. et al., 2018, Astrobiology, 18, 133
Morgenstern O. et al., 2013, J. Geophys. Res. Atmos., 118, 1028
Morton T. D., Bryson S. T., Coughlin J. L., Rowe J. F., Ravichandran G., Petigura E. A., Haas M. R., Batalha N. M., 2016, ApJ, 822, 1
O'Malley-James J. T., Kaltenegger L., 2017, MNRAS, 469, L26
Palmer T. N., 2012, Q. J. R. Meteorol. Soc., 138, 841
Proedrou E., Hocke K., 2016, Earth Planets Space, 68, 96
Quintana E. V. et al., 2014, Science, 344, 277
Rajpurohit A. S., Reylé C., Allard F., Homeier D., Schultheis M., Bessell M. S., Robin A. C., 2013, A&A, 556, A15
Roney P., 1965, J. Atmos. Terr. Phys., 27, 1177
Schwieterman E. W. et al., 2018, Astrobiology, 18, 663
Seager S., 2014, Proc. Natl. Acad. Sci., 111, 12634
Seager S., Kuchner M., Hier-Majumder C. A., Militzer B., 2007, ApJ, 669, 1279
Segura A., Walkowicz L. M., Meadows V., Kasting J., Hawley S., 2010, Astrobiology, 10, 751
Shields A. L., Meadows V. S., Bitz C. M., Pierrehumbert R. T., Joshi M. M., Robinson T. D., 2013, Astrobiology, 13, 715
Shields A. L., Ballard S., Johnson J. A., 2016, Phys. Rep., 663, 1
Showman A. P., Polvani L. M., 2011, ApJ, 738, 71
Sing D. K. et al., 2011, A&A, 527, A73
Spiegel D. S., Fortney J. J., Sotin C., 2014, Proc. Natl. Acad. Sci., 111, 12622
Telford P. J. et al., 2013, Geosci. Model Dev., 6, 161
Thompson S. E. et al., 2018, ApJS, 235, 38
Tilley M. A., Segura A., Meadows V., Hawley S., Davenport J., 2019, Astrobiology, 19, 64
Todorov K. O., Deming D., Burrows A., Grillmair C. J., 2014, ApJ, 796, 100
Tompkins A. M., 2000, Mon. Weather Rev., 128, 1521
Turbet M., Forget F., Head J. W., Wordsworth R., 2017, Icarus, 288, 10
Walker J. C. G., Hays P. B., Kasting J. F., 1981, J. Geophys. Res. Oceans, 86, 9776
Walters D. et al., 2017, Geosci. Model Dev. Discuss., 2017, 1
Weiss L. M., Marcy G. W., 2014, ApJ, 783, L6
Wild O., Zhu X., Prather M. J., 2000, J. Atmos. Chem., 37, 245
Yang J., Abbot D. S., 2014, ApJ, 784, 155

## SUPPORTING INFORMATION

Supplementary data are available at *MNRAS* online.

## APPENDIX A: PHYSICAL DESCRIPTION OF NUMERICAL EXPERIMENTS

## APPENDIX B: ADDITIONAL 3D CHEMISTRY FIELDS

Please note: Oxford University Press is not responsible for the content or functionality of any supporting materials supplied by the authors. Any queries (other than missing material) should be directed to the corresponding author for the article.

This paper has been typeset from a TEX/LATEX file prepared by the author.